PCCP

PAPER

View Article Online
View Journal | View Issue

Cite this: *Phys. Chem. Chem. Phys.*, 2016, **18**, 2608

Nanocrystalline anatase TiO_2/reduced graphene oxide composite films as photoanodes for photoelectrochemical water splitting studies: the role of reduced graphene oxide†

Andreia Morais,[a] Claudia Longo,[a] Joyce R. Araujo,[b] Monica Barroso,[c] James R. Durrant[d] and Ana Flavia Nogueira*[a]

Received 3rd November 2015,
Accepted 4th December 2015

DOI: 10.1039/c5cp06707c

www.rsc.org/pccp

Nanocrystalline TiO_2 and reduced graphene oxide (TiO_2/RGO) composite films were prepared by combining a sol–gel method with hydrothermal treatment, employing titanium isopropoxide ($Ti(O^iPr)_4$) and graphene oxide (GO) as starting materials. Although several reports in the literature have explored the benefits of RGO addition in titania films for photocatalysis and water splitting reactions, the role of RGO in the composite is always described as that of a material that is able to act as an electron acceptor and transport electrons more efficiently. However, in most of these reports, no clear evidence for this "role" is presented, and the main focus is deviated to the improved efficiency and not to the reasons for said efficiency. In this study, we employed several techniques to definitively present our understanding of the role of RGO in titania composite films. The TiO_2/RGO composite films were characterized by X ray diffraction, Raman spectroscopy, microscopy and electrochemical techniques. In photoelectrochemical water splitting studies, the $TiO_2/RGO_{(0.1\%)}$ photoelectrodes showed the highest photocurrent density values (0.20 mA cm^{-2} at 1.23 V_{RHE}) compared to other electrodes, with an increase of 78% in relation to pristine TiO_2 film (0.11 mA cm^{-2} at 1.23 V_{RHE}). The transient absorption spectroscopy (TAS) results indicated increases in the lifetime and yield of both the photogenerated holes and electrons. Interestingly, the $TiO_2/RGO_{(0.1\%)}$ film exhibited the best charge generation upon excitation, corroborating the photoelectrochemical data. We proposed that in films with lower concentrations (<0.1 wt%), the RGO sheets are electron acceptors, and a decrease in the charge recombination processes is the immediate consequence. Thus, both holes and electrons live longer and contribute more effectively to the photocurrent density.

Introduction

Since Fujishima and Honda[1] (1972) published the first report of the photoelectrochemical splitting of water into hydrogen (H_2) and oxygen (O_2) over titanium dioxide or titania (TiO_2) photoanodes, different types of semiconductors have been developed and evaluated as candidate photoelectrodes for solar-driven hydrogen production.[2] Among these diverse semiconductors, TiO_2 is still one of the more studied as a photocatalyst, due to its excellent thermal, chemical and photochemical stability, its insolubility in water and its availability on a large scale. The photoactivity of this material is observed only when it is irradiated with ultraviolet light, which corresponds to only approximately 4% of incident solar energy.[3] Many strategies to improve the absorption of TiO_2 in the visible part of the solar spectrum have been accomplished; these include the introduction of impurities (*e.g.* nitrogen atoms) to change the band gap of TiO_2[4] and sensitization with particles as CdS, CdSe or CdSTe.[5] The development of new architectures, such as nanotubes,[6] nanowires,[7] nanorods[8] and nanoparticles,[9] is also an alternative to improve the performance of TiO_2 by increasing the semiconductor surface area and/or electronic transport.

Another challenge for the more efficient use of TiO_2 as a photocatalyst for water splitting or pollutant oxidation is to

[a] *Chemistry Institute, University of Campinas (UNICAMP), P. O. Box 6154, 13083-970, Campinas, São Paulo, Brazil. E-mail: anaflavia@iqm.unicamp.br*
[b] *National Institute of Metrology, Quality and Technology, Av. Nossa Sra. das Graças, 50, 25250-020, Duque de Caxias, Rio de Janeiro, Brazil*
[c] *Debye Institute for Nanomaterials Science, Utrecht University, Bolognalaan 10 VII, 3584 CJ Utrecht, Netherlands*
[d] *Department of Chemistry, Imperial College London, South Kensington Campus, London SW7 2AZ, UK*

† Electronic supplementary information (ESI) available: Synthesis of reduced graphene oxide and its characterization by XRD, Raman, XPS, TGA, FEG-SEM and HRTEM; characterization of TiO_2 and TiO_2/RGO films by optical microscopy and UV-vis spectroscopy; electrochemical properties of these films by cyclic voltammetry, chronoamperometry and electrochemical impedance spectroscopy and IPCE analysis. See DOI: 10.1039/c5cp06707c

improve the electronic transport that occurs by diffusion in the oxide semiconductor film.[10] In this case, the diffusion of the photogenerated charge carriers is relatively "slow" on conventional TiO_2 films; therefore, the charge recombination probability increases, resulting in a decrease in the photocurrent density and photocatalytic efficiency for several reactions.[11] An interesting alternative to reduce this effect is the incorporation of carbon-based materials into nanocrystalline TiO_2 films such as carbon nanotubes,[12] carbon black[13] and carbon quantum dots.[14] Our group has successfully demonstrated the use of boron or nitrogen-doped hollow carbon in TiO_2(P25) films for photoelectrochemical studies[15] and TiO_2/MWCNT as photoanodes in dye sensitized solar cells.[16] Another carbonaceous material that has been widely used for this application is graphene, due to its high surface area (2630 $m^2\ g^{-1}$), photodegradation resistance, optical transparency ($\sim$97.7%) and high charge mobility values (200 000 $cm^2\ V^{-1}\ s^{-1}$).[17]

Graphene oxide (GO), a graphene derivative, is an electrically insulating material and usually exhibits a rich assortment of oxygen-containing groups such as carboxylic, hydroxyl, carbonyl, and epoxide groups. The electrical conductivity of GO can be increased by reduction and partial restoration of the sp^2-hybridized network; the resulting product, also known as reduced graphene oxide (RGO), has properties similar to graphene (although the reduction methods do not fully restore the ideal characteristics of graphene sheets).[17,18]

However, the combination of TiO_2 nanoparticles and RGO sheets remains a good strategy to improve the photocatalytic performance of semiconductor oxides for several reactions. The electron-accepting ability presented by the RGO sheets can be used to enhance the electron transport properties of the TiO_2 films.[19–22] For instance, Ng *et al.*[23] reported that TiO_2(P25)–RGO nanocomposite electrodes showed significant activity for the photocatalytic decomposition of 2,4-dichlorophenoxyacetic acid, and Bell *et al.*[24] proposed the use of these nanocomposite films for photoelectrochemical water splitting. These researchers observed a significant increase in photocurrent density values compared to pure TiO_2 film for all wavelengths in the ultraviolet region. Li and Cui[25] observed that TiO_2/RGO (0.2 wt%) reached a hydrogen production rate of 43.8 μmol h^{-1}, which was 1.6 times greater than that of a TiO_2 sample. Recently, our research group demonstrated that the presence of RGO in TiO_2/CdS films can increase methanol production from the photoreduction of carbon dioxide (CO_2),[26] whereas TiO_2/Cu_2O films may favor the photocatalytic degradation of methylene blue dye.[27] In addition, films of TiO_2/RGO applied as electron transport layers improved the efficiency of P3HT/PC_{61}BM organic solar cells.[28] Although the advantages of the incorporation of RGO sheets in the TiO_2 matrix are well known, unfortunately, a detailed understanding of the role of graphene and its derivatives is still very controversial and scarce in the literature. Some studies suggest that the RGO can facilitate electron injection and assist in electron transport,[29,30] whereas other studies have reported that RGO can act as a sensitizer in semiconductor oxide films.[31–33] For this reason, there is a need for a more detailed and definitive investigation of the role of RGO sheets in the TiO_2 matrix, and how this successful combination of materials has improved the photocatalytic performance of several oxides.

Herein, we report a facile route for the growth of nanocrystalline TiO_2 particles on RGO sheets by combining a sol–gel method with hydrothermal treatment, employing titanium isopropoxide ($Ti(O^iPr)_4$) and graphene oxide (GO) as starting materials. In photoelectrochemical water splitting studies, the influence of the addition of different amounts of RGO to the TiO_2 matrix was investigated by cyclic voltammetry, chronoamperometry and electrochemical impedance spectroscopy (EIS) analysis. Charge generation/recombination dynamics (electrons and holes) using transient absorption spectroscopy (TAS) was also employed to correlate the excited state dynamics with the electrochemical reactions at the photoanode.

Experimental

Materials

All reagents were of analytical grade and used without further purification. The natural graphite powder was purchased from Nacional de Grafite LTDA (code: Micrograf 99507UJ). All other reagents were purchased from Sigma-Aldrich. The fluorine-doped tin oxide (FTO) conductive glasses (Hartford glass, $R_s \leq 10\ \Omega\ sq^{-1}$) were cleaned ultrasonically with water–detergent solution, water, acetone, methanol and isopropanol successively in ultrasonic baths for 15 min. All substrates were dried with compressed nitrogen gas and treated with UV-ozone for 20 min.

Preparation of nanocrystalline TiO_2/RGO pastes

The synthesis of reduced graphene oxide (RGO) from graphite and its characterization by XRD, Raman spectroscopy, TGA, FEG-SEM and HRTEM is described in the ESI† (Fig. S2–S6, Tables S1 and S2). In the ESI,† detailed characterizations of graphite and graphene oxide (precursors in the synthesis of the RGO sheets) are also available. Moreover, X-ray photoelectron analyses (XPS) were used to determine the chemical composition of the graphite, graphite oxide and RGO-hydrothermal samples. Pastes containing nanocrystalline TiO_2 particles and RGO (TiO_2/RGO) were prepared using titanium isopropoxide ($Ti(O^iPr)_4$) and GO as starting materials. First, the 1.8% w/w GO dispersion (5.8 g) was dispersed in 0.10 mol L^{-1} HNO_3 solution (100 mL) using an ultrasonic bath for 30 min. Moreover, glacial acetic acid (3.5 mL) was added to $Ti(O^iPr)_4$ (16 mL) under stirring in a closed system that was previously purged with nitrogen. The TiO_2 precursors were then injected into the acid GO dispersion and heated and maintained at 80 °C for 8 h in reflux; subsequently, the suspension was autoclaved at 220 °C for 12 h. Finally, using a rotary evaporator, the resulting homogeneous suspension was concentrated to a colloidal paste, composed of 11 wt% nanocrystalline TiO_2 particles and 5.0 wt% RGO (designed as TiO_2/$RGO_{(5\%)}$). Furthermore, polyethylene glycol (PEG, M_w = 2000) was added in a proportion of 40% of the total TiO_2 weight.

A TiO_2 paste was also prepared by the same procedure in the absence of RGO. Pastes containing different relative amounts

of RGO, TiO_2/$RGO_{(0.01\%)}$, TiO_2/$RGO_{(0.05\%)}$, TiO_2/$RGO_{(0.1\%)}$, TiO_2/$RGO_{(0.5\%)}$, TiO_2/$RGO_{(1\%)}$ and TiO_2/$RGO_{(2\%)}$ were prepared using adequate amounts of TiO_2/$RGO_{(5\%)}$ and the TiO_2 pastes (see Fig. S1 in the ESI†). The resulting pastes were stored in screw-threaded glass bottles.

Preparation of TiO_2/RGO films

For the preparation of the electrodes, an aliquot of TiO_2 or TiO_2/RGO paste was spread onto a fluorine-doped tin oxide conductive substrate (glass-FTO) by the doctor blading technique, using adhesive tape (Scotch Magic Tape, 3M, thickness <50 μm) to control the film thickness. After drying in air for 30 min, the films were heated at 350 °C for 2 h with a heating rate of 10 °C min^{-1}. The resulting films were uniform, without any noticeable cracks; the average thicknesses were measured with a Taylor/Hobson Form Talysurf 50 profilometer. These samples were cut into 1×1.5 cm^2 pieces, resulting in electrodes with geometrical active areas of 1.0 cm^2. These electrodes were stored in a dry atmosphere.

Characterization of TiO_2/RGO films

X ray diffraction (XRD) measurements were performed using a Shimadzu XRD7000 diffractometer (40 kV, 30 mA) with Cu (λ = 1.54178 Å) irradiation in the 2θ range of 5–80°. The Raman spectra were obtained using a confocal Raman spectrometer (model T64000 – Jobin Yvon – USA) equipped with a CCD (charge coupled device) detector and an Olympus BTH 2 microscope. The excitation laser was set at 514 nm with a 20-fold magnification objective lens.

Optical microscopy images were taken with a Nikon Eclipse 5i (H5505, Nikon, Japan) microscope equipped with a Digital Sight Camera System (DS-Fi1 Nikon, Japan) and using an objective lens with a magnification of 20×. Field emission gun scanning electron microscopy (FEG-SEM) images were taken on a FEI Inspect F50 microscope at a voltage of 10 kV. High-resolution transmission electron microscopy (HRTEM) images were acquired using a JEM 3010 URP microscope at an accelerating voltage of 300 kV.

Photoelectrochemical studies of TiO_2/RGO films

Electrochemical measurements were carried out in an Autolab® model PGSTAT 10N potentiostat/galvanostat (Eco Chemie). The electrochemical impedance spectroscopy (EIS) measurements were carried out in an Autolab® model PGSTAT-302-N potentiostat/galvanostat with a frequency response analyzer FRA module (Eco Chemie). The EIS measurements were performed at the open circuit potential with a sinusoidal voltage perturbation of 10 mV, in the frequency range from 50 kHz to 5 mHz.

A conventional three-electrode photoelectrochemical cell, consisting of glass-FTO|TiO_2 or glass-FTO|TiO_2/RGO as the working electrode (active area of 1 cm^2), a platinum wire as the counter electrode and Ag/AgCl in a KCl solution (3.0 mol L^{-1}) as the reference electrode, was used in the experiments. An aqueous H_2SO_4 solution (0.5 mol L^{-1}) was used as the electrolyte. The measured $E_{Ag/AgCl}$ potential values were converted to the reversible hydrogen electrode potentials (E_{RHE}) using the Nernst equation and considering the standard potential of the reference electrode, $E^0_{Ag/AgCl}$, which corresponds to 0.21 V_{RHE} at 25 °C:

$$E_{RHE} = E^0_{Ag/AgCl} + E_{Ag/AgCl} + 0.059\ pH \quad (1)$$

The photoelectrochemical cell was placed in an optical bench consisting of an Oriel Xe (Hg) 250 W lamp coupled to an AM 1.5G filter (Oriel) and collimating lenses. The light intensity was calibrated with an optical power meter, model 1830-C (Newport), to 100 mW cm^{-2}; however, no correction was made to discount reflection and transmission losses.

Transient absorption spectroscopy

The investigation of the recombination dynamics of the photogenerated electrons and holes in the TiO_2 and TiO_2/RGO films was performed using transient absorption spectroscopy (TAS). All transient absorption measurements on the μs–s time scale were performed using a Nd:YAG laser (Continuum Surelite I-10) as the UV excitation source (355 nm, ~200 μJ cm^{-2} per pulse, typically 1 Hz repetition rate and 6 ns pulse width). A 75 W xenon lamp (Hamamatsu) was used as the continuous light source (probe beam). The lamp wavelengths were selected, using a monochromator, at 460 nm and 900 nm for lifetime monitoring of the photogenerated holes and electrons, respectively. The second monochromator after the sample was used to reduce the emission intensity and scattering from the laser before reaching the Si PIN photodiode. The detection system was comprised of a silicon photodiode (Hamamatsu Photonics) coupled to a digital oscilloscope (Tektronix TDS220) triggered by the laser excitation pulse. The transient decay data is the result of averaging between 300 laser shots. The TiO_2 and TiO_2/RGO films were placed in a sealed quartz cuvette and were thoroughly degassed with nitrogen prior to use. In this study, ΔOD means the transient absorption change.

Results and discussion

Structural and morphological properties of TiO_2 and TiO_2/RGO nanoparticles and films

The morphological characterization of the TiO_2 and TiO_2/RGO materials was investigated through FEG-SEM and HRTEM. Fig. 1(a) shows that TiO_2 particles have varied sizes and shapes, with an average diameter of ~15 nm. These features were also observed in the composite samples with different RGO concentrations. For the TiO_2/RGO composite, HRTEM and FEG-SEM images indicate that the RGO sheets are completely covered and decorated with TiO_2 nanoparticles (Fig. 1(b–d)). This strong interaction between the RGO sheets and the TiO_2 nanoparticles is important to achieve a good electronic coupling between these two materials.

The XRD patterns obtained for the TiO_2 and TiO_2/$RGO_{(5\%)}$ films and powder TiO_2/$RGO_{(5\%)}$ nanocomposite are presented in Fig. 2(a). The diffractograms also include the Joint Committee on Powder Diffraction Standards (JCPDS) information for the anatase and rutile phases, 21-1272 and 21-1276, respectively. The Raman spectra obtained for the TiO_2 and TiO_2/$RGO_{(5\%)}$ films are presented in Fig. 2(b).

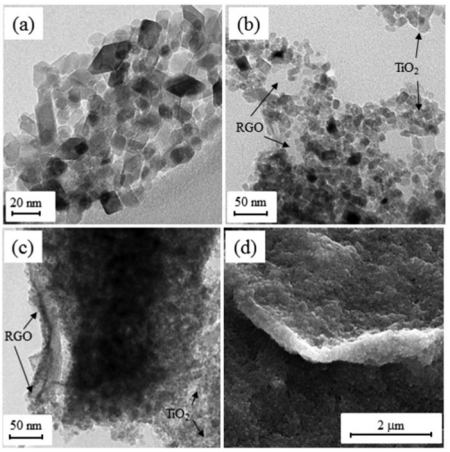

Fig. 1 HRTEM images of the powders of (a) TiO_2 particles, (b and c) TiO_2/$RGO_{(5\%)}$ nanocomposites and (d) FEG-SEM image of the powder TiO_2/$RGO_{(5\%)}$ nanocomposite.

The XRD pattern of the TiO_2/$RGO_{(5\%)}$ nanocomposite (powder) showed the presence of TiO_2 crystalline structure, predominantly the anatase allotropic form.[34] This information can also be observed in the TiO_2 and TiO_2/$RGO_{(5\%)}$ films; however, the signals are less intense. The diffraction peaks marked with an asterisk (*) correspond to the crystalline phases of the FTO substrate. Comparison of the XRD diffraction peaks for the TiO_2/$RGO_{(5\%)}$ composite and the pure TiO_2 films demonstrates that the presence of RGO did not change the TiO_2 preferential crystal orientations. The typical diffraction peaks of carbon species, observed at $2\theta = 25^\circ$ in Fig. S5(a) (ESI†), are not observed in the composite, probably due to the relatively low RGO low amount.[35]

The Raman results showed specific vibration modes located around 150 cm^{-1} (E_g), 200 cm^{-1} (E_g), 400 cm^{-1} (B_{1g}), 510 cm^{-1} ($B_{1g} + A_{1g}$) and 630 cm^{-1} (E_g), indicating the presence of anatase phase.[36] No peak assigned to the rutile or brookite phase was observed, which is consistent with the XRD results. For the TiO_2/$RGO_{(5\%)}$ film, two additional prominent peaks centered at 1324 cm^{-1} (D band) and 1600 cm^{-1} (G band) are also observed in the Raman spectrum, suggesting that the structure of RGO was maintained in the composite. Furthermore, an I_D/I_G ratio of 1.09, higher than that of the RGO-hydrothermal sample (I_D/I_G = 1.02) (see Fig. S5(b) in the ESI†) was observed, suggesting structural disorder related to the strong interaction between the TiO_2 nanoparticles and the RGO sheets after the reduction process by the hydrothermal method.[37]

Fig. 3 shows images of the surfaces of the electrodes obtained by optical microscopy and FEG-SEM. While a transparent film was obtained from the deposition of the pristine TiO_2 suspension on glass-FTO, a dark film resulted from the TiO_2/$RGO_{(5\%)}$ suspension (Fig. 3(a)). Films with different TiO_2/RGO relative amounts were obtained from suspensions prepared by the mixture of pristine TiO_2 and TiO_2/$RGO_{(5\%)}$ suspensions; the images clearly show that the composite films become darker as the relative RGO concentration increases. Furthermore, different morphologies can be observed for the films of TiO_2 and TiO_2/RGO composites. Images of all the nanocomposite films are available in Fig. S7 in the ESI.† The surface and cross-section images (Fig. 3(f and g)) show that the TiO_2/$RGO_{(5\%)}$ film has a high porosity, interconnected pores and a thickness of around 5.3 μm.

Fig. 4 shows the UV-visible absorption spectra of the TiO_2, TiO_2/$RGO_{(0.1\%)}$, TiO_2/$RGO_{(2\%)}$ and TiO_2/$RGO_{(5\%)}$ films.

A significant increase in the absorption at wavelengths shorter than 400 nm is assigned to TiO_2 (~3.2 eV).[38] For the composites,

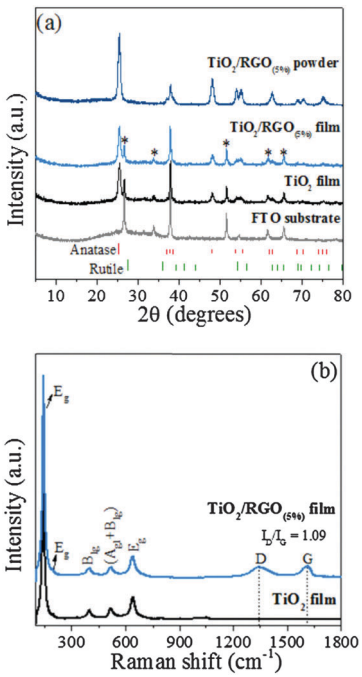

Fig. 2 (a) XRD patterns for the FTO substrate, TiO_2, TiO_2/$RGO_{(5\%)}$ films and powder TiO_2/$RGO_{(5\%)}$ nanocomposite. (b) Raman spectra for the TiO_2 and TiO_2/$RGO_{(5\%)}$ films.

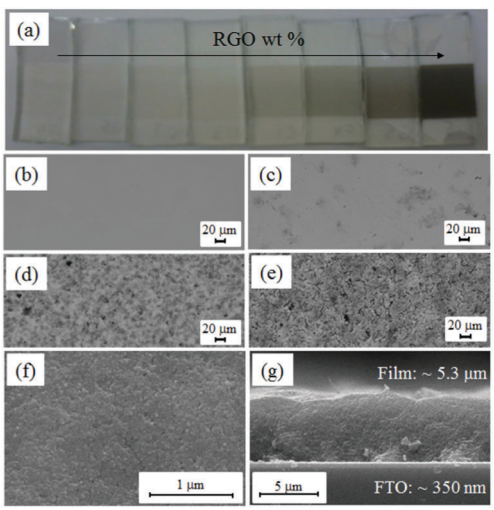

Fig. 3 (a) Images of the TiO_2 and TiO_2/RGO films. Optical microscopy images of the (b) TiO_2, (c) TiO_2/$RGO_{(0.1\%)}$, (d) TiO_2/$RGO_{(2\%)}$ and (e) TiO_2/$RGO_{(5\%)}$ films. FEG-SEM images of the (f) surface and (g) cross-section of the TiO_2/$RGO_{(5\%)}$ film.

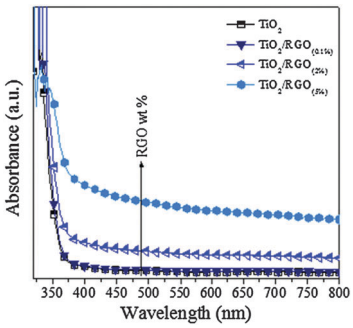

Fig. 4 UV-visible absorption spectra for the TiO_2, TiO_2/$RGO_{(0.1\%)}$, TiO_2/$RGO_{(2\%)}$ and TiO_2/$RGO_{(5\%)}$ films.

the light absorption remains unchanged for relative RGO concentrations of <1.0 wt%. On the other hand, there is a marked increase in the light absorption intensity in the entire investigated region when the RGO concentration is greater than 1.0 wt%. In this case, light scattering must also be considered, mainly in the visible and near-infrared regions. The films become darker, and this behavior will have important implications in the photoelectrochemical response of these films, as will be discussed in the last section. Tauc plots were used to determine the optical band gap in the films. The results showed that the addition of RGO decreases the band gap energy (E_g) from 3.6 eV (pristine TiO_2) to 3.4 eV (sample with 5.0 wt% of RGO). This small variation, although positive, is not expected to play a major role in the photocurrent values.

Transient absorption spectroscopy studies of the TiO_2/RGO films

TAS measurements were performed to study the charge carrier dynamics (holes and electrons) after Nd:YAG laser excitation (350 μJ cm^{-2}) in the ultraviolet region (355 nm) for the TiO_2 and TiO_2/RGO composites with RGO relative concentrations of 0.1, 2 and 5 wt%. Fig. 5(a) and (b) show the spectra obtained using the probe wavelengths at 460 nm (mainly photohole absorption) and 900 nm (mainly photoelectron absorption).

The observed transient absorption decays in the TiO_2 and TiO_2/RGO films are attributed to electron–hole recombination when the experiments are carried out under nitrogen in the absence of any chemical scavengers. This behavior was also observed by Tang *et al.*[39] when studying the dynamics of the charge carriers in the nitrogen-doped-TiO_2 (nc-N-TiO_2) films. In all the nanocomposite films containing RGO sheets, we observed an increase in the amplitude of the long lived 460 nm (photohole) signals and also an increase in the amplitude of the long lived 900 nm (photoelectron) signals in comparison with the pristine TiO_2 film. The optical density variation (ΔOD) observed is proportional to the number of charge carriers photogenerated, and it is significantly larger for the nanocomposites than for the pristine TiO_2 films. This is a strong indication of a decrease in the charge recombination.

The increase in the yield of the holes is clear: considering the RGO sheets as electron acceptors, the charge recombination reaction between the electrons and holes is minimized.

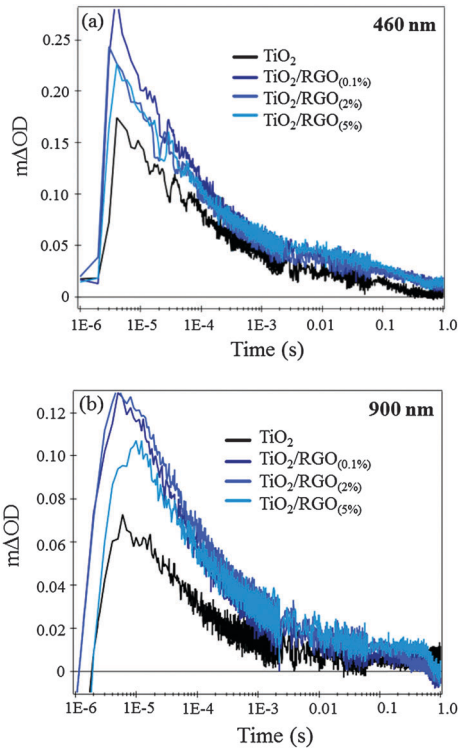

Fig. 5 Transient absorption spectra of (a) photoholes (460 nm) and (b) photoelectrons (900 nm) in TiO_2, TiO_2/$RGO_{(0.1\%)}$, TiO_2/$RGO_{(2\%)}$ and TiO_2/$RGO_{(5\%)}$ films after Nd:YAG laser excitation in the ultraviolet region (355 nm), in nitrogen atmosphere and in the absence of chemical scavengers.

In addition, the origin of the increase in the 900 nm signal is less clear and may be derived from the absorption of RGO electrons. According to Meng *et al.*,[40] who used TAS as an additional tool to understand the photocatalytic improvement of TiO_2/α-Fe_2O_3 composite for water oxidation, the mechanism is associated with mobile electrons, which are initially created in semiconductors and quickly transfer to the RGO sheet, wherein they diffuse into trap states in the RGO on a time scale of picoseconds. These trapped electrons reach the photoelectrode, leading to an increase in the photocurrent.

Photoelectrochemical studies of the TiO_2/RGO films

Pristine TiO_2 and TiO_2/RGO films were employed as photoanodes in photoelectrochemical water splitting studies in 0.5 mol L^{-1} H_2SO_4 medium. The cyclic voltammograms, obtained in the dark and under illumination (100 mW cm^{-2}, AM 1.5G) through the electrolyte–electrode interface (EE), are shown in Fig. 6.

In a wide potential range (−0.4 to 2.4 V_{RHE}), only a well-defined peak at *ca.* −0.29 V_{RHE} is observed during the anodic sweep; this can be attributed to the oxidation of Ti(III) (hydr)-oxide species (>Ti(OH)) on the TiO_2 surface. During the cathodic sweep, a reduction peak of the Ti(IV) (hydr)oxide species (>$Ti(OH)_2$) was also observed at potentials lower than 0.06 V_{RHE} (see Fig. S9 in the ESI†).[41] In the dark, the electrodes exhibited a very small capacitive current; for potentials greater than 2.0 V_{RHE}, the current is related to the oxygen evolution

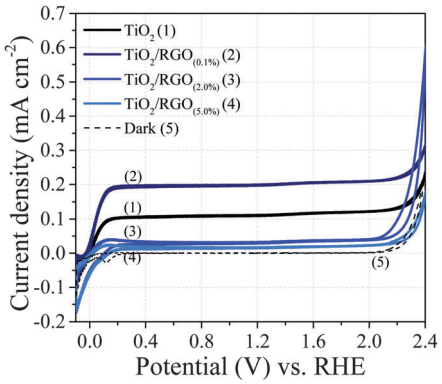

Fig. 6 Cyclic voltammograms obtained using the TiO_2, $TiO_2/RGO_{(0.1\%)}$, $TiO_2/RGO_{(2\%)}$ and $TiO_2/RGO_{(5\%)}$ films as photoanodes in 0.5 mol L^{-1} H_2SO_4, in the dark and under illumination.

reaction (OER). Furthermore, a well-defined peak was observed at around 0.09 V_{RHE} during the cathodic sweep. The presence of this peak is widely discussed in the literature, and it has been associated with the reduction of species at surface states located below the semiconductor conduction band, mainly due to the presence of electronic traps in the films. At potentials below 0 V_{RHE}, the hydrogen evolution reaction (HER) also occurs.[42]

In illumination conditions, as expected for n-type semiconductor electrodes, all the films showed an anodic photocurrent. According to Fig. 5(b), the photocurrent is directly dependent on the RGO concentration in the TiO_2 composite electrode. At 1.23 V_{RHE} (standard potential for OER) for the pristine TiO_2 electrode, the photocurrent corresponds to 0.11 mA cm^{-2}; for the composite electrodes, it increased with RGO relative concentration, and the maximum value of 0.20 mA cm^{-2} was observed for the composite containing 0.1 wt% RGO. The photocurrent decreased sharply to 0.02 mA cm^{-2} for the $TiO_2/RGO_{(5\%)}$ film. The variation of the photocurrent density values (at 1.23 V_{RHE}) with the relative concentration of RGO in the TiO_2/RGO films electrodes is shown in Fig. S11 in the ESI.† The $TiO_2/RGO_{(0.1\%)}$ electrode has a maximum $IPCE_{(350nm)}$ of around 18% (see Fig. S12 in the ESI†), which is higher in comparison to other electrodes.

It is noteworthy that none of the onset potentials ($\sim$0 V_{RHE}) of the voltammograms changed, and thus it is possible to discount any catalytic effect of the RGO sheets. It is very important to emphasize that these measurements were also repeated using the same photoelectrodes and experimental conditions, but with the use of a UV blocking filter ($<$400 nm). The voltammogram profiles for all the photoelectrodes were similar to the results obtained in the dark (compare Fig. S10(a) and S13 in the ESI†). Thus, we can discard the idea that the RGO sheets, at least in our study, are acting as sensitizers in the TiO_2 film. Kumar *et al.*[43] have calculated the work function of rGO sheets as a function of the oxygen concentration. Thus, we expect that the work function for our sample is about 5.4 eV. The energy level of the conduction band of TiO_2 is about 4.4 eV.[44] This provides additional information that the energy levels do not allow electron transfer from the RGO to the conduction band of the titania film. However, in a recent report, Bharad *et al.*[45] reported a mechanism for water splitting reactions based on TiO_2 sensitization by RGO and N-doped RGO. It is clear that this subject needs a deeper investigation to check the feasibility of electron transfer from the graphene-based materials to the titania films.

The photoresponse ability and long-term stability of the same photoelectrodes were determined using chronoamperometric measurements under potentiostatic control at 1.23 V_{RHE}, as shown in Fig. 7. In general, the photoelectrodes exhibited a prompt photo-response under intermittent irradiation with high reproducibility during numerous ON/OFF cycles, as well as good electrochemical stability during continuous irradiation for 1 h. It is noteworthy that the photocurrent density values obtained by chronoamperometry were very similar to the cyclic voltammetry results.

The electrochemical and photoelectrochemical properties of these electrodes were also investigated by electrochemical impedance spectroscopy (EIS) measurements, carried out in H_2SO_4 aqueous solution at open circuit potential (V_{OC}), in the dark and under illumination. Fig. 8 presents the Nyquist and the Bode diagrams of the EIS data obtained for the TiO_2 and TiO_2/RGO photoelectrodes (represented by symbols), with their mathematical adjustments (represented by solid lines) obtained using Boukamp software with the suggested equivalent circuit (inset in Fig. 8(a)). At V_{OC}, in the dark, all these electrodes exhibited similar electrochemical impedance spectra, with high impedance values and undefined time constants (Fig. 8(a) and (b)). Under illumination conditions, the general impedance value decreases considerably, and a well-defined capacitive arc and two time

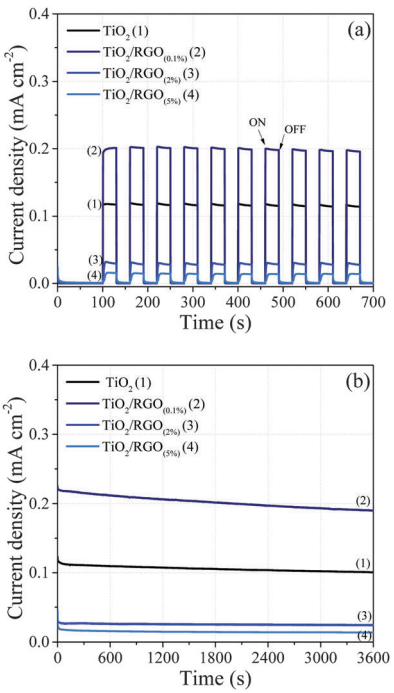

Fig. 7 Time-dependent photocurrent density under potentiostatic control at 1.23 V_{RHE} under intermittent irradiation using a manual chopper with intervals of 30 s in the dark and 30 s under irradiation (a) and under continuous irradiation (b) for the TiO_2, $TiO_2/RGO_{(0.1\%)}$, $TiO_2/RGO_{(2\%)}$ and $TiO_2/RGO_{(5\%)}$ photoelectrodes in 0.5 mol L^{-1} H_2SO_4.

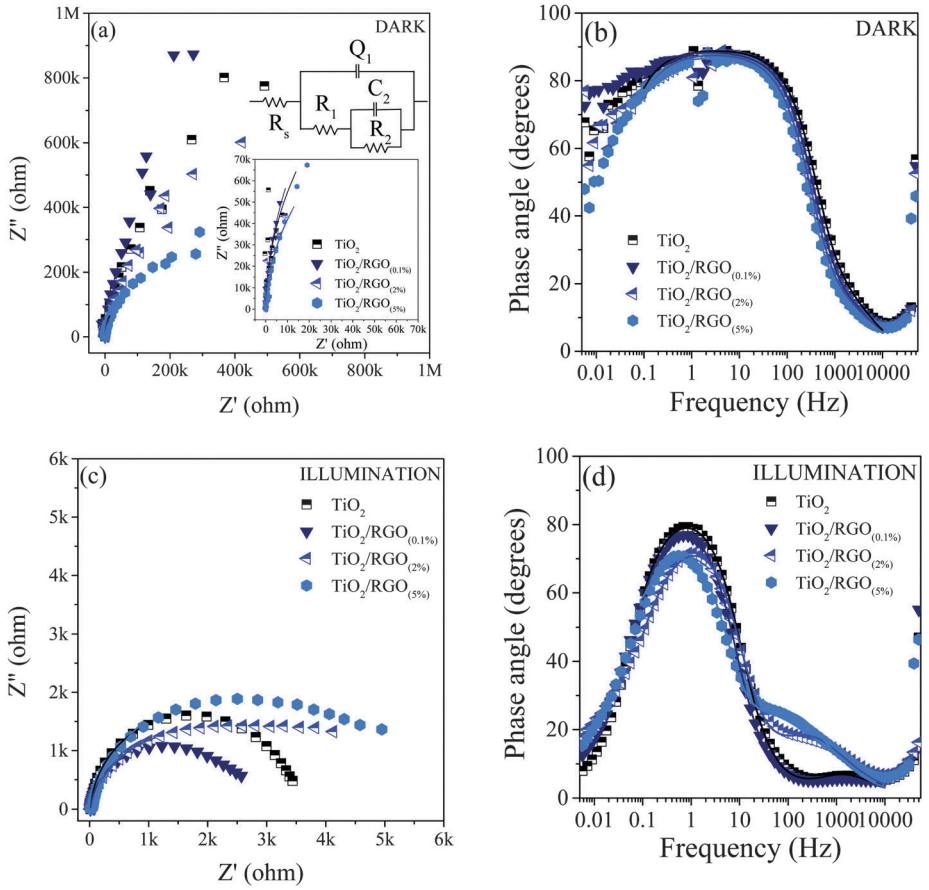

Fig. 8 (a and b) Nyquist and (c and d) Bode (phase angle *versus* frequency) diagrams of the EIS data obtained for the TiO_2, TiO_2/$RGO_{(0.1\%)}$, TiO_2/$RGO_{(2\%)}$ and TiO_2/$RGO_{(5\%)}$ photoelectrodes at open circuit potential in 0.5 mol L^{-1} H_2SO_4 in the dark (a) and (b) and under illumination (c) and (d). The symbols correspond to the experimental data and the solid lines represent the fits obtained using Boukamp software in the inset of (a). The equivalent circuit is inseted in (a).

constants can be displayed for all the photoelectrodes (Fig. 8(c) and (d)). An equivalent circuit $R_s(Q_1(R_1(R_2C_2)))$ has been proposed for fitting the EIS data.[15,46,47] All the adjustments have been made in the frequency range from 10 kHz to 0.1 Hz, due to the high dispersion of the data.

The proposed equivalent circuit (inset in Fig. 8(a)) considers a series resistance element (R_s), which includes the FTO resistance, the resistance related to the ionic conductivity of the electrolyte and the external contact resistance. The semiconductor|electrolyte interface can be represented by the capacitance at the Helmholtz layer (Q_1) on the electrolyte side and the charge transfer resistance (R_1). The electron transport in the semiconductor bulk can be represented by the resistance (R_2) and the capacitance (C_2) at the TiO_2 surface states. The contribution of the RGO sheets on the TiO_2 surface can also be visualized by these two parameters. Moreover, in photoelectrodes formed by nanostructured semiconductors, the capacitance is commonly well represented by a CPE, in which admittance depends on the parameters Y_o and n (n is a constant ranging from $0 \leq n \leq 1$). In this case, the semiconductor electrode|electrolyte interface cannot be represented by simple circuits such as RC or R(RC); thus, the resultant capacitance should not vary with applied potential, as assumed by the Mott–Schottky relationship.[15,46,47]

The parameters obtained by fitting the EIS spectra with the equivalent circuit depicted in Fig. 7(a) are presented in Table 1.

The circuit element values obtained in the dark are similar among the photoelectrodes, with R_s values of *ca.* 14 Ω, capacitances (Q_1 and C_2) of *ca.* 15 μF and resistances (R_1 and R_2) of 10 Ω and 312 kΩ on average, respectively. Under illumination, the TiO_2/$RGO_{(0.01\ to\ 0.1\%)}$ electrodes showed R_1 (5.3 to 4.8 Ω) and R_2 (3.0 to 2.4 kΩ) values lower than the pure TiO_2 electrode (R_1 = 5.8 Ω and R_2 = 689 kΩ). The capacitance values ($Q_1 \sim 316$ μF and $C_2 \sim 1010$ μF) were higher compared to the pristine TiO_2 electrode (Q_1 = 166 μF and C_2 = 689 μF). This behavior indicates a higher charge accumulation at the interface and faster electron transport, associated with the presence of RGO.

Note that a low concentration of RGO in the TiO_2 film (<0.1 wt%) does not significantly change the light absorption (see Fig. S8 in the ESI†). On the other hand, for RGO concentrations above 0.5 wt% in the TiO_2 films, the photocurrent density values decrease; many factors may be related to this process. Under illumination, the TiO_2/$RGO_{(0.5\ to\ 5\%)}$ electrodes showed increasing values of R_1 and R_2: 6.2 to 63 Ω and 2.2 to 6.2 kΩ, respectively. In addition, there was a marked decrease in the values in one of the capacitances (C_2), from 835 to 367 μF. This can be directly related to the presence of agglomerations

Table 1 Parameters obtained by fitting the impedance spectra of the TiO_2 and TiO_2/RGO photoelectrodes in 0.5 mol L^{-1} H_2SO_4, using the equivalent circuit $R_s(Q_1(R_1(R_2C_2)))$[a]

				Q_1				
	Photoelectrodes	χ^2 (10^{-3})	R_s (Ω)	Y_o (μF s^{n-1})	n	R_1 (Ω)	R_2 (kΩ)	C_2 (μF)
Dark	TiO_2	6.0	12	13	0.99	11	324	11
	$TiO_2/RGO_{(0.01\%)}$	0.5	12	15	0.99	11	291	16
	$TiO_2/RGO_{(0.05\%)}$	4.6	15	11	0.99	8.8	417	16
	$TiO_2/RGO_{(0.1\%)}$	0.3	13	14	0.98	8.9	409	13
	$TiO_2/RGO_{(0.5\%)}$	0.6	13	16	0.98	10	383	14
	$TiO_2/RGO_{(1\%)}$	0.2	16	16	0.97	8.7	236	15
	$TiO_2/RGO_{(2\%)}$	0.4	14	16	0.97	9.8	212	14
	$TiO_2/RGO_{(5\%)}$	0.8	16	16	0.95	8.6	223	16
Illumination	TiO_2	0.2	14	166	0.78	5.8	3.6	689
	$TiO_2/RGO_{(0.01\%)}$	0.4	14	223	0.75	5.3	3.0	1083
	$TiO_2/RGO_{(0.05\%)}$	0.2	14	320	0.72	5.1	2.6	1218
	$TiO_2/RGO_{(0.1\%)}$	0.2	13	316	0.74	4.8	2.4	1010
	$TiO_2/RGO_{(0.5\%)}$	0.2	12	317	0.72	6.2	2.2	835
	$TiO_2/RGO_{(1\%)}$	0.3	15	337	0.70	14	2.4	451
	$TiO_2/RGO_{(2\%)}$	0.6	14	363	0.70	26	3.4	358
	$TiO_2/RGO_{(5\%)}$	1.3	14	471	0.68	63	6.2	367

[a] Fitting performed with Boukamp software. The symbols R, C and Q account for resistance, capacitance and the constant phase element (CPE), respectively.

of RGO sheets that block light absorption in the TiO_2 nanoparticles. The light-block effect contributes to the decay of the photocurrent density values, corroborating the EIS data.

As the amount of RGO increases, charge recombination becomes more important, and this can explain our best result obtained by the films containing 0.1 wt% of RGO. Moreover, as the concentration of RGO increases, the films become darker; this seems to negatively affect the charge generation. As shown previously in Fig. 4, as the RGO content increases, the light absorption by the titania nanoparticles is compromised, decreasing the photoactivity towards water oxidation and also the charge generation. It is important to point out that the correspondence between the TAS and the photoelectrochemical studies. The sample that gave rise to the best performance in the water oxidation process ($TiO_2/RGO_{(0.1\%)}$) also originated the highest yield for both charge carriers.

Conclusions

Although several reports of the photocatalytic effect and water splitting reactions at the surface of TiO_2/RGO nanocomposite have been published in the last few years, a clear understanding of the RGO role is lacking. For instance, the sensitization effect of RGO in the titania film was not observed in our study. Moreover, the energy levels of both materials do not allow charge transfer from the RGO to the titania conduction band. However, the opposite can be accomplished. In the photoelectrochemical water splitting investigation, the $TiO_2/RGO_{(0.1\%)}$ photoelectrode showed the highest photocurrent density value (0.20 mA cm^{-2} at 1.23 V_{RHE}) compared to the other electrodes, with an increase of 78% in relation to the pristine TiO_2 films (0.11 mA cm^{-2} at 1.23 V_{RHE}). However, at higher concentrations (0.5 to 5.0 wt%), the photocurrent density values sharply decrease, probably due to the darkening and the agglomerations of RGO sheets in these films, which deteriorated the electrical parameters, as observed by EIE. The TAS results indicated an increase in lifetime and yield of both the photogenerated holes and electrons. Interestingly, the $TiO_2/RGO_{(0.1\%)}$ film exhibited the best charge generation upon excitation, corroborating the photoelectrochemical studies. We propose that in films with lower concentrations (<0.1 wt%), the positive effect of the RGO sheets is due to their ability to accept and transfer electrons from TiO_2. The immediate consequence is a decrease in charge recombination, observed by the increase in the photogeneration of holes and electrons in TAS decays and a significant improvement in the photocurrent density in photoelectrochemical water splitting.

Acknowledgements

The authors thank LNNano/LNLS for the FEG-SEM and HRTEM images, Inmetro for the XPS analysis, and INEO, CNPq and FAPESP (fellowship 2010/18656-1 and 2011/51593-6) for financial support.

Notes and references

1 A. Fujishima and K. Honda, *Nature*, 1972, **238**, 37–38.
2 M. G. Walter, E. L. Warren, J. R. McKone, S. W. Boettcher, Q. X. Mi, E. A. Santori and N. S. Lewis, *Chem. Rev.*, 2010, **110**, 6446–6473.
3 M. Ni, M. K. H. Leung, D. Y. C. Leung and K. Sumathy, *Renewable Sustainable Energy Rev.*, 2007, **11**, 401–425.
4 H. Fakhouri, J. Pulpytel, W. Smith, A. Zolfaghari, H. R. Mortaheb, F. Meshkini, R. Jafari, E. Sutter and F. Arefi-Khonsari, *Appl. Catal., B*, 2014, **144**, 12–21.
5 G. J. Ai, R. Mo, H. Xu, Q. Chen, S. Yang, H. X. Li and J. X. Zhong, *J. Power Sources*, 2015, **280**, 5–11.

6 A. M. Mohamed, A. S. Aljaber, S. Y. AlQaradawi and N. K. Allam, *Chem. Commun.*, 2015, **51**, 12617–12620.
7 J. Z. Su and L. J. Guo, *RSC Adv.*, 2015, **5**, 53012–53018.
8 C. Fabrega, T. Andreu, A. Tarancon, C. Flox, A. Morata, L. Calvo-Barrio and J. R. Morante, *Int. J. Hydrogen Energy*, 2013, **38**, 2979–2985.
9 S. H. Liu and H. R. Syu, *Appl. Energy*, 2012, **100**, 148–154.
10 B. O'Regan, J. Moser, M. Anderson and M. Grätzel, *J. Phys. Chem.*, 1990, **94**, 8720–8726.
11 A. Westwood and R. Leary, *Carbon*, 2011, **49**, 741–772.
12 K. Dai, T. Y. Peng, D. N. Ke and B. Q. Wei, *Nanotechnology*, 2009, **20**, 125603.
13 Y. Cong, X. K. Li, Z. J. Dong, G. M. Yuan, Z. W. Cui and J. Zhang, *Mater. Lett.*, 2015, **138**, 200–203.
14 M. X. Sun, X. Q. Ma, X. Chen, Y. J. Sun, X. L. Cui and Y. H. Lin, *RSC Adv.*, 2014, **4**, 1120–1127.
15 K. Ranganathan, A. Morais, I. Nongwe, C. Longo, A. F. Nogueira and N. J. Coville, *J. Mol. Catal. A: Chem.*, 2015, in press.
16 A. de Morais, L. M. D. Loiola, J. E. Benedetti, A. S. Goncalves, C. A. O. Avellaneda, J. H. Clerici, M. A. Cotta and A. F. Nogueira, *J. Photochem. Photobiol., A*, 2013, **251**, 78–84.
17 Q. J. Xiang, J. G. Yu and M. Jaroniec, *Chem. Soc. Rev.*, 2012, **41**, 782–796.
18 S. F. Pei and H. M. Cheng, *Carbon*, 2012, **50**, 3210–3228.
19 X. Y. Zhang, H. P. Li, X. L. Cui and Y. H. Lin, *J. Mater. Chem.*, 2010, **20**, 2801–2806.
20 B. W. Wang, Q. M. Sun, S. H. Liu and Y. P. Li, *Int. J. Hydrogen Energy*, 2013, **38**, 7232–7240.
21 F. Y. Pei, Y. L. Liu, L. Zhang, S. P. Wang, S. G. Xu and S. K. Cao, *Mater. Res. Bull.*, 2013, **48**, 2824–2831.
22 F. Y. Pei, G. L. Liu, S. G. Xu, J. Lu, C. X. Wang and S. K. Cao, *Int. J. Hydrogen Energy*, 2013, **38**, 2670–2677.
23 Y. H. Ng, I. V. Lightcap, K. Goodwin, M. Matsumura and P. V. Kamat, *J. Phys. Chem. Lett.*, 2010, **1**, 2222–2227.
24 N. J. Bell, H. N. Yun, A. J. Du, H. Coster, S. C. Smith and R. Amal, *J. Phys. Chem. C*, 2011, **115**, 6004–6009.
25 H. Li and X. L. Cui, *Int. J. Hydrogen Energy*, 2014, **39**, 19877–19886.
26 J. E. Benedetti, D. R. Bernardo, A. Morais, J. Bettini and A. F. Nogueira, *RSC Adv.*, 2015, **5**, 33914–33922.
27 B. M. Almeida, M. A. Melo, J. Bettini, J. E. Benedetti and A. F. Nogueira, *Appl. Surf. Sci.*, 2015, **324**, 419–431.
28 A. Morais, J. P. C. Alves, F. A. S. Lima, M. Lira-Cantu and A. F. Nogueira, *J. Photonics Energy*, 2015, **5**, 057408.
29 N. L. Yang, J. Zhai, D. Wang, Y. S. Chen and L. Jiang, *ACS Nano*, 2010, **4**, 887–894.
30 T. F. Yeh, J. Cihlar, C. Y. Chang, C. Cheng and H. S. Teng, *Mater. Today*, 2013, **16**, 78–84.
31 M. Q. Yang and Y. J. Xu, *J. Phys. Chem. C*, 2013, **117**, 21724–21734.
32 Y. H. Zhang, N. Zhang, Z. R. Tang and Y. J. Xu, *ACS Nano*, 2012, **6**, 9777–9789.
33 A. J. Du, Y. H. Ng, N. J. Bell, Z. H. Zhu, R. Amal and S. C. Smith, *J. Phys. Chem. Lett.*, 2011, **2**, 894–899.
34 Y. H. Zhang, Z. R. Tang, X. Z. Fu and Y. J. Xu, *ACS Nano*, 2010, **4**, 7303–7314.
35 Y. H. Zhang, Z. R. Tang, X. Fu and Y. J. Xu, *ACS Nano*, 2011, **5**, 7426–7435.
36 S. D. Perera, R. G. Mariano, K. Vu, N. Nour, O. Seitz, Y. Chabal and K. J. Balkus, *ACS Catal.*, 2012, **2**, 949–956.
37 B. T. Liu, Y. J. Huang, Y. Wen, L. J. Du, W. Zeng, Y. R. Shi, F. Zhang, G. Zhu, X. H. Xu and Y. H. Wang, *J. Mater. Chem.*, 2012, **22**, 7484–7491.
38 J. J. Fan, S. W. Liu and J. G. Yu, *J. Mater. Chem.*, 2012, **22**, 17027–17036.
39 J. W. Tang, A. J. Cowan, J. R. Durrant and D. R. Klug, *J. Phys. Chem. C*, 2011, **115**, 3143–3150.
40 F. K. Meng, J. T. Li, S. K. Cushing, J. Bright, M. J. Zhi, J. D. Rowley, Z. L. Hong, A. Manivannan, A. D. Bristow and N. Q. Wu, *ACS Catal.*, 2013, **3**, 746–751.
41 F. Y. Oliva, L. B. Avalle, E. Santos and O. R. Camara, *J. Photochem. Photobiol., A*, 2002, **146**, 175–188.
42 T. Berger, D. Monllor-Satoca, M. Jankulovska, T. Lana-Villarreal and R. Gomez, *ChemPhysChem*, 2012, **13**, 2824–2875.
43 P. V. Kumar, M. Bernardi and J. C. Grossman, *ACS Nano*, 2013, **7**, 1638–1645.
44 H. J. Tang, C. M. Hessel, J. Y. Wang, N. L. Yang, R. B. Yu, H. J. Zhao and D. Wang, *Chem. Soc. Rev.*, 2014, **43**, 4281–4299.
45 P. A. Bharad, K. Sivaranjani and C. S. Gopinath, *Nanoscale*, 2015, **7**, 11206–11215.
46 B. Klahr, S. Gimenez, F. Fabregat-Santiago, T. Hamann and J. Bisquert, *J. Am. Chem. Soc.*, 2012, **134**, 4294–4302.
47 T. Lopes, L. Andrade, F. Le Formal, M. Gratzel, K. Sivula and A. Mendes, *Phys. Chem. Chem. Phys.*, 2014, **16**, 16515–16523.

